Applied Radiation and Isotopes 68 (2010) 59–65

Contents lists available at ScienceDirect

Applied Radiation and Isotopes

journal homepage: www.elsevier.com/locate/apradiso

Patient specific treatment planning for systemically administered radiopharmaceuticals using PET/CT and Monte Carlo simulation

J.J. Grudzinski [a,*], H. Yoriyaz [b], P.M. DeLuca Jr.[a], J.P. Weichert [a]

[a] Department of Medical Physics, University of Wisconsin School of Medicine and Public Health, 1111 Highland Ave, Madison, WI, USA
[b] Instituto de Pesquisas Energeticas e Nucleares, Cidade Universitaria, Sao Paulo, Brazil

ARTICLE INFO

Article history:
Received 16 June 2009
Received in revised form
24 September 2009
Accepted 25 September 2009

Keywords:
Radionuclide treatment planning
PET/CT
Monte Carlo
Patient specific dosimetry

ABSTRACT

The efficacy of systemically administered radiopharmaceuticals depends on the physiological path of the targeting molecule and the physical characteristics of the attached radionuclide. NM404 is a candidate for patient specific dosimetry because it can be used concurrently for both diagnosis and therapy. Radiolabeling NM404 with [^{124}I] affords the possibility of performing noninvasive PET imaging while [^{131}I] allows for radiotherapy. Patient specific dosimetry for radiation treatment planning for NM404 uses serial PET/CT data and Monte Carlo. [^{124}I]NM404 PET helps to determine the organ at risk by which the maximum injected activity of [^{131}I]NM404 will depend. The subsequent work uses a software interface (SCMS) to convert patient PET/CT data of a liver metastasis into a Monte Carlo environment for radiation transport analysis. Thereby, the dosimetry within the liver and tumor during both diagnostic and therapeutic procedures was determined. The results showed that per MBq injected of [^{124}I] and [^{131}I], the tumor receives an average of 1.2 and 1.5 mGy, respectively, while the liver receives 0.031 and 0.022 mGy, respectively.

1. Introduction

1.1. Nuclear imaging with iodine

Due to its physiologically driven accumulation in the thyroid, iodine was the first and remains the most used radionuclide for diagnostic and therapeutic nuclear medicine (Williams et al., 2008). Specifically, ^{131}I ($t_{1/2}$=8.0 days; Betas—606 keV (89%), Gamma and X-ray 364 keV (81%)) has been traditionally used in the treatment of thyroid cancer because of the organ energy deposition and physical half-life (Brans et al., 2007; Ott, 1996; O'Donoghue and Wheldon, 1996). Furthermore, the gamma emissions from ^{131}I permit single photon emission computed tomography (SPECT) imaging during therapy (Thomas, 2002). ^{131}I is an effective imaging nuclide in SPECT, but lacks the precision and accuracy of ^{124}I ($t_{1/2}$=4.2 days; Betas—1532 keV (11%); 2135 keV (11%), Gamma and X-ray–511 keV (46%); 603 keV (61%); 1691 keV (11%)) when used in positron emission tomography (PET).

PET offers higher sensitivity than SPECT due to coincidence-detection. The use of SPECT collimators, while increasing spatial resolution, causes a decrease in sensitivity. For comparable scan times, PET has better image quality than SPECT and regions of interest (ROI) are more accurate in PET compared to SPECT. A potential solution for diminished sensitivity is scanning a smaller field of view. Conversely, a smaller field of view leads to increased scan times which make full-body scans with SPECT very difficult (Rahmim and Zaidi, 2008). Comparing the two radioisotopes of iodine, ^{124}I and ^{131}I, ^{124}I is capable of achieving higher spatial resolution images than ^{131}I, 6.6 mm FWHM compared to 14.1 mm FWHM (Rault et al., 2007) which contributes to more precise dosimetric calculations (Pentlow et al., 1991; Flux et al., 2006). Lastly, attenuation correction in SPECT imaging is much more elaborate to implement than in PET that leads to longer image processing times (Rahmim and Zaidi, 2008). The combined advantages of higher sensitivity, higher resolution and improved quantification make PET imaging with ^{124}I more useful than ^{131}I SPECT when implementing patient specific dosimetry (Flux et al., 2006). Though ^{131}I SPECT has been used extensively to perform patient specific dosimetry (Dewaraja et al., 2009; Brown et al., 2008; Gear et al., 2007; O'Donoghue et al., 2002), ^{124}I is becoming increasingly used in clinical PET and has advantages when doing ^{131}I therapy treatment planning (Sgouros et al., 2004; Eschmann et al., 2002; Ravinder et al., 2007).

Combining PET and X-ray computed tomography (CT) for ^{124}I-PET/CT hybrid scanning can further improve quantitative accuracy in estimating ^{131}I dosimetry (Bai et al., 2003; Kinahan et al., 1998; Flux et al., 2006; Dingli et al., 2006). The overlaying of a PET defined volume on a CT volume anatomically confirms the locations of increased activity uptake of possible lesions (Delbeke

* Corresponding author. Tel.: +1 608 347 6524.
E-mail address: grudzinski@wisc.edu (J.J. Grudzinski).

0969-8043/$ - see front matter © 2009 Elsevier Ltd. All rights reserved.
doi:10.1016/j.apradiso.2009.09.070

et al., 2009). An ROI around an organ on the CT data is defined and the activity on the coinciding PET data is summed up. The CT data, which contains innate electron density information, is also used for attenuation correction so that activity within an ROI is more accurately determined. After all PET corrections are applied, the true concentration of a particular tracer (Bq/cm^3) within an ROI is estimated. If serial ^{124}I-PET/CT scans are acquired, the pharmacokinetics of the tracer within an organ can be used to estimate the dosimetry of therapeutic ^{131}I (Strand et al., 1993). The isoteric relationship between the two radioisotopes of iodine ensures identical physiochemical properties.

1.2. Iodine: a candidate for patient specific dosimetry

Any tumor targeting pharmaceutical that can be radioiodinated has the potential to be used for patient specific dosimetry. One example is NM404, a tumor-targeting molecule that is selectively retained in malignant cells (Pinchuk et al., 2006). When it is radiolabeled with ^{124}I, its selective retention can be noninvasively imaged using PET scanning (Weichert et al., 2005). Subsequently, when NM404 is radiolabeled with ^{131}I, its selective retention in malignant cells allows for solid tumor therapy. By radiolabeling NM404 with different isotopes of iodine to assume diagnostic or therapeutic functions, NM404 is an example of a *diapeutic* molecular tracer that shows promise for patient specific treatment planning.

The patient specific treatment planning process is a three step approach: diagnostic serial ^{124}I-PET/CT imaging, simulated ^{131}I radiotherapy after ^{131}I dosimetry is estimated, and real ^{131}I radiotherapy. By performing serial PET/CT scans of a patient over time, the patient specific pharmacokinetics of an agent within the body is determined. The PET data in conjunction with the simulated therapy provide the information to determine the organ at risk (OAR) during radiotherapy. Considering the pharmacokinetics and toxicity threshold of the OAR, the subsequent radiotherapy of the patient is optimized based on an estimated maximum allowable injected activity.

The mode of clearance is important with any tracer used for targeted radiotherapy because it can dictate the maximum permissible activity administered to a patient. In targeted radiotherapy, it is essential to deliver therapeutic doses to a tumor while sparing normal surrounding tissues. The organs within the excretion pathway of a targeting agent are often the normal tissues of concern. High renal excretion of the radiotherapy agent can severely limit its use since renal and bladder tissues are relatively radiosensitive. Various radiolabled peptides such as ^{166}Ho-DOTMP (Breitz et al., 2003) and ^{90}Y-DOTATOC (Barone et al., 2005; Pauwels et al., 2005) require continuous renal function monitoring and sometimes irrigation as to avoid normal tissue complications. It has even been shown that neglecting dose-rate underestimates the dose-effect on the kidneys. However, NM404 is excreted primarily (~5% renal clearance) via the hepatobiliary pathway which includes the liver and gallbladder. In our study, we investigated a case that represented a liver metastasis and used liver toxicity as an endpoint: $TD_{5/5}$ 1/3 of 50 Gy (Emami et al., 1991). The liver toxicity was corrected using the formalism of biological effective dose which takes into the dose-rate. The purpose of this work was to use PET/CT imaging in combination with Monte Carlo radiation transport to accurately calculate the dosimetry of ^{124}I-NM404 and ^{131}I-NM404 in a case that resembles a liver metastasis. The novelty of this work is found in the translation of human PET/CT data into the Monte Carlo environment for treatment planning of systemically administered radiopharmaceutical therapy based on liver toxicity avoidance.

2. Methods and materials

2.1. Data acquisition

The data that were used for liver dosimetry analysis of $^{124/131}$I were obtained from a patient, low-activity, ^{124}I-NM404 PET/CT scan. The innate contrast between liver and surrounding organs provided by the CT data aided in using a threshold method to segment the liver. Being calibrated for Bq/ml, the PET data defined the spatial concentration of the tracer within the liver.

The data were obtained on the GE Advance clinical PET/CT scanner (Waukesha, WI). For PET acquisition, the patient was injected with 55.5 MBq (55.5 MBq/15 μg) of ^{124}I-NM404 and scanned 6, 30, and 54 h post-injection using eight different bed positions of 8 min each. The ^{124}I was purchased from IBA Molecular. The PET data were then reconstructed using 2D ordered subset expectation maximization (OSEM) with two iterations, 35 subsets, and a 5 mm post filter. (Doll et al., 2004). OSEM is a commercially available iterative reconstruction algorithm that provides PET images that are of higher quality than filtered back projection (FBP) reconstruction. The clinical CT acquisition protocol consisted of a technique using 140 kVp, 120 mA current, and 1121 ms exposure. The CT data were reconstructed using FBP and subsequently applied to the PET data for attenuation correction.

2.2. Image processing

Before the PET/CT data were translated into the Monte Carlo environment, extensive image processing was performed. The software interface that implemented the PET/CT data into a Monte Carlo environment, MCNPX (Los Alamos National Laboratory), required image manipulation that was accomplished using Amira (Visage Imaging; Carlsbard, CA).

2.3. ROI quantification

Using Amira, an image processing software package, a three-dimensional ROI—volume of interest (VOI)—was drawn around the entire liver using the whole body CT scan. A liver metastasis was simulated by creating a VOI of a "tumor" volume within the liver VOI (Fig. 1). This resulted in an image mask that consisted of three materials: liver, tumor, and "outside of liver". After multiplying the whole body PET image data at each time point by the image mask, the PET data which overlaid the liver and tumor was extracted out of the original data. In a human, about 5% of the injected activity of NM404 is taken up in the liver while solid tumors can attain 15% of the total injected activity (data not

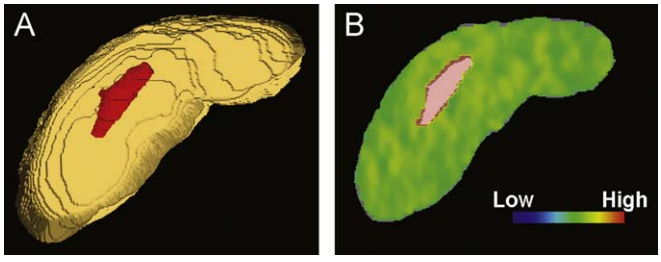

Fig. 1. (A) is a voxelized representation in the axial direction of a tumor (red) within a normal liver (beige). The tumor is indicated with an arrow (B) is an axial slice of the PET distribution within the liver and tumor. The tumor is of highest activity illustrated by the color pink. With the assistance of SCMS, this voxelized phantom and PET distribution can be implemented within the Monte Carlo environment. (For interpretation of the references to color in this figure legend, the reader is referred to the webversion of this article.)

published). Due to this discrepancy, the PET data that overlaid the tumor were artificially scaled. After re-sampling the CT data to that of the dimensions of the PET volume, the physiological distribution of NM404 within a liver and tumor was ready to be implemented into MCNPX (Ferrari and Gualdrini, 2007). This was accomplished using an interface called SCMS (Yoriyaz et al., 2001). MCNPX is described below.

2.4. SCMS—segmented phantom construction software for the MNCP radiation transport simulation

The SCMS interface was the tool used to construct a voxelized phantom within the combinatorial geometry environment of MCNPX. After converting the CT mask data into ASCII format, the SCMS interface converted the voxels into a three dimensional lattice of cells that consisted of a $86 \times 70 \times 21$ ($3 \times 3 \times 8.5$ mm) matrix. This coarse matrix assisted in the variance reduction of the Monte Carlo environment. Each structure (i.e. liver, tumor, or outside) was defined by numerous universes consisting of cells with different materials and densities. The liver and tumor (soft tissue) were assigned densities of 1.04 g/cm^3 while the outside (water) was given a density of 1.0 g/cm^3. In contrast, the ASCII PET data were used to specify the location of the isotropic sources within the different cells. The entire source distribution created a probability density function (pdf) that was weighted by the PET intensity values (Bq/mL).

2.5. MCNPX simulations

The Monte Carlo radiation transport code MCNPX was used to simulate the dose distribution caused by $^{124/131}$I radiation decay. Since the PET data only estimates the bio-distribution of ^{124}I, the ^{131}I bio-distribution was assumed to be the same but with a half-life difference correction. For each radionuclide, multiple simulations were performed to account for the different decay modes: gamma rays, beta rays, positrons, etc. The dose contribution from photons and electrons were performed separately for both nuclides. ^{124}I also has a contribution from positrons which was included. For both nuclides, the decay branching ratios defined the MCNPX source definition. Each branching ratio had a discretely defined energy and probability associated with it (Stabin and da Luz, 2002). As a proof of principle, the full beta spectrum for each radionuclide was discritized into their respective beta energy bins. A discrete probability density function was used instead of a continuous one.

The *F8 or pulse height tally scores the energy (MeV) of a photon, electron, or positron as it enters or leaves a cell. A positive energy tally occurs from particles that enter a cell, and a negative energy tally occurs when a particle leaves a cell. After simulating enough source particles (N_{src}=1×10^9) that resulted in a variance within voxel of less than 5%, each cell has a resulting average MeV/N_{src} (energy/source particle) that was converted to internal dose (Gy/N_{src}) by dividing it by the mass of each cell and multiplying it by a conversion factor. From both ^{131}I and ^{124}I, there were multiple dose matrices which corresponded to each mode of decay. The cumulative energy from each particle (photon, electron, and positron) was weighed by its branching ratio for its respective nuclide. Ultimately, a dose matrix of Gy/N_{src} (Eqs. (2) and (3)) for each nuclide was created using Matlab (2006). From there, it was possible to compute the total dose to the liver and tumor and display it.

2.6. Tracer kinetics using OLINDA/EXM

In dosimetry studies, the dose to particular organs is commonly represented by mGy/MBq$_{\text{injected}}$ activity. To achieve this in our study, it was necessary to use pharmacokinetic data of NM404 within the liver and tumor. By evaluating serial PET/CT data of ^{124}I-NM404 at 6 h post injection and extrapolating to time=0 h, it was concluded that 6.5% of the injected activity was taken up in the liver. Although tumor uptake has been found to range between 5 and 25%ID/g with NM404 in over 40 preclinical solid tumor models, 15% was chosen as a representative value for tumor uptake for purposes of this dose simulation. In order to derive the true dose for patient specific dosimetry, the number of nuclear disintegrations that took place within the liver and tumor (residence time, $\tilde{A}$) was determined. Because the tracer clears biologically and the radionuclide decays physically, it was important to consider the effective half-life. For the proceeding analysis, it was assumed that the liver and tumor achieved maximum uptake instantaneously at the time of tracer injection and are cleared with a mono-exponential decay. If 1 MBq of either iodine isotope is injected, 21.5% is taken up in the liver and tumor and is cleared with the same biological decay constant (λ_{bio}).

$$\tilde{A} = 0.215 * A_0 \int_0^{\infty} e^{-\lambda_{eff} t} dt = \frac{0.215 \cdot A_0}{\lambda_{eff}} \tag{1}$$

where A_0 is the initial injected activity,

$$\lambda_{eff} = \lambda_{bio} + \lambda_{phys} \text{and} \lambda = \frac{\ln 2}{T_{1/2}}$$

The biological clearance constant (λ_{bio}) of the liver of a particular patient was determined by using the PET/CT data over three time points. To simplify the analysis, the biological clearance constant of the tumor was assumed to be the same as the liver. By decay correcting the data, and fitting the data to a mono-exponential decay function using least squares analysis in OLINDA/EXM 1.0 (Stabin et al., 2005), the biological clearance constant for liver and tumor was derived, 0.00371 h^{-1} (Fig. 2).

Because ^{131}I and ^{124}I have different physical half-lives, they will have different accumulated activities within the liver and tumor. By using Eq. (1), each radionuclide's accumulated activity was calculated. The cumulated activity for ^{131}I, $\tilde{A}(^{131}I)$, was 1.75 GBq s/MBq injected while $\tilde{A}(^{124}I)$ was 1.18 GBq s/MBq injected. The total dose for each nuclide is the dose matrix with units of Gy/N_{src} multiplied by the accumulated activities of each nuclide. The total dose per 1MBq injected for both ^{131}I and ^{124}I is derived from the sum

$$\frac{D}{A_0} = \left(\frac{\text{mGy}}{1\,\text{MBq}}\right)_{^{131}I} = \tilde{A}(^{131}I)\left(\frac{\text{Gy}}{N_{src}}\right)_{^{131}I} \tag{2}$$

Fig. 2. Decay corrected data for NM404 clearance from the liver using OLINDA/EXM. The best fit line exemplifies a mono-exponential decay function with the biological decay constant (λ_{bio}) of 0.00371 h^{-1}.

$$\frac{D}{A_0} = \left(\frac{\text{mGy}}{1\,\text{MBq}}\right)_{^{124}I} = \tilde{A}(^{124}I)\left(\frac{\text{Gy}}{N_{src}}\right)_{^{124}I} \quad (3)$$

of Eqs. (2) and (3). It was now possible to determine the dose to the liver and tumor using different injected activities.

2.6.1. Extension of absorbed to the biologically effective dose (BED) formalism

The absorbed dose in radiotherapy is a physical quantity that describes the energy imparted in tissue with no mention of biological effect. It is widely understood that the dose rate can have a substantial influence on the effect caused to tissue. Due to the variation in dose-rate, it cannot be assumed that equal physical doses from different dose-rates will result in the same effect. The linear-quadratic (LQ) model of cell survival has been adopted to derive an equivalent parameter that may be used to represent the effects of both components: total dose and dose-rate. The LQ formalism given in Eq. (4) applies to radiation delivered in a single acute dose as in external beam therapy (Roberson and Buchsbaum, 1995; Lazarescu and Battista, 1997; Barone et al., 2005; Yang and Xing, 2005). The model gives the fraction of cells surviving the irradiation (SF) as a function of the dose delivered, D:

$$\ln(SF) = -\alpha D - \beta D^2 \quad (4)$$

It is assumed that insufficient time is available for cellular repair to take place during the irradiation; however, for the high dose-rates and short treatment times of external beam therapy this is largely appropriate. Conversely, when treatments are carried out at lower dose-rates as with ^{131}I therapy, the treatment duration can be protracted to a timescale over which repair can take place, resulting in a reduction in the level of damage caused. At lower dose-rates there will generally be a greater temporal separation between events, and the probability increases that sub-lethal damage will be repaired before the β-type double-hit damage is formed. The α component of damage, which involves single-hit cell kill, is independent of dose-rate. Therefore, the β term of Eq. (4) which is affected by changes in dose-rate, and a dose-protraction or Lea-Catcheside factor (Sachs et al., 1997; Brenner et al., 1998; Hobbs and Sgouros, 2009), G, has been incorporated to introduce a correction to the level of damage due to the relationship between dose-rate and repair (Dale and Carabe-Fernandez, 2005; Dale, 1996, 1985, 1989; Bodey et al., 2004).

$$\ln(SF) = -\alpha D - \beta G D^2 \quad (5)$$

The biologically effective dose (BED) takes into account the temporal pattern of dose delivery. It is a dose normalization that reduces the total dose to infinitesimally small fractions which affords the possibility of comparing different radiation modalities of different dose-rates. For a continuous irradiation at an exponentially decaying dose-rate such, G is given by

$$G = \frac{\lambda}{\lambda+\mu} \quad (6)$$

where λ is the constant of dose-rate decay, and μ is the constant of sub-lethal damage repair (Dale, 1985; Millar, 1991). The assumption is made that both these decays are mono-exponential, and that the dose-rate decays to zero. The BED for targeted radionuclide therapy is then given by

$$BED_{TRT} = D_{TRT}\left(1 + \frac{D_{TRT}\lambda}{(\mu+\lambda)(\alpha/\beta)}\right) \quad (7)$$

2.6.2. Treatment planning proof of concept

To estimate the tumor dose from ^{131}I-NM404, we first analyzed the ^{124}I-NM404 PET/CT data and simulated ^{131}I-NM404 therapy. We performed a treatment planning proof of concept in which the maximum permissible ^{131}I-NM404 was determined by liver toxicity avoidance, $BED_{5/5}$ 1/3. A dose volume histogram (DVH) such as Fig. 3 is a quantitative summary of the absorbed dose distribution from ^{131}I that illustrates the overall percent coverage of dose. A maximum permissible dose can be computed by avoiding the liver toxicity of $TD_{5/5}$ 1/3 of 50 Gy from Emami et al. which is converted to a $BED_{5/5}$ 1/3 of 62 Gy using Table 1. The maximum permissible injected activity also took into account the BED imparted from an already administered imaging activity of 370 MBq of ^{124}I-NM404. The resulting tumor BED was found by multiplying the maximum permissible activity by the maximum ^{131}I-NM404 tumor dose per injected activity (mGy/MBq) that encompasses 100% of the tumor volume, Fig. 3, and converting it to BED using Table 1.

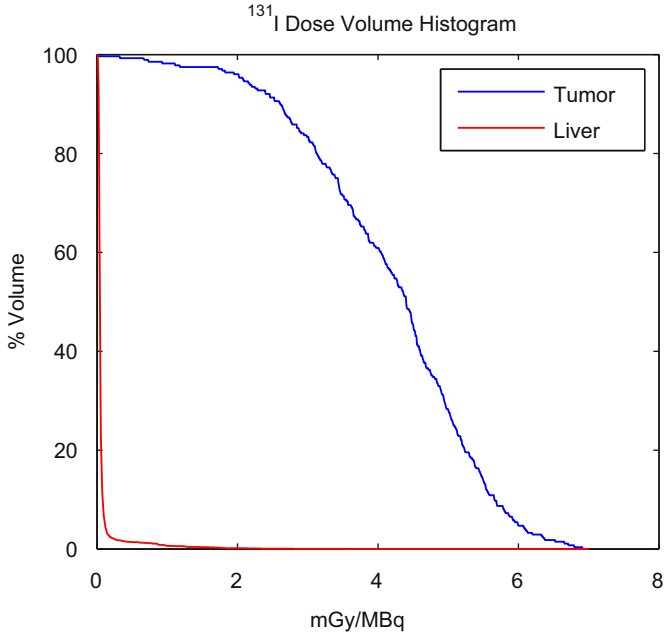

Fig. 3. A dose volume histogram (DVH) illustrating the volumetric difference between the absorbed dose of ^{131}I in the liver and tumor.

Table 1
The radiobiological parameters that are used to compute the biologically effective dose (BED) for the liver and tumor (Dale, 1996).

	α/β (Gy)	μ (h^{-1})	λ_{bio} (h^{-1})	^{131}I λ_{phys}	^{124}I λ_{phys}
Tumor	10	1.4	0.0037	0.0036	0.0069
Liver	3	0.5	0.0037	0.0036	0.0069

3. Results

Fig. 4 shows the results of the Monte Carlo dose simulations. It should be noted that the increased levels of dose found in (A) and (B) of Fig. 4 was due to the close proximity of the tumor which causes a "cross-fire" effect. The dose within the tumor or liver was uniform. However, the tumor retained 15% of the injected activity compared to 5.9% within the liver which contributed too much of the liver dose as well as the tumor dose. Though very minor, there was also a residual amount of dose delivered to a volume outside the liver. In the body, this dose would be imparted to the right kidney or possibly the lungs. The results of the Monte Carlo dose simulations corrected for BED are found in Table 2.

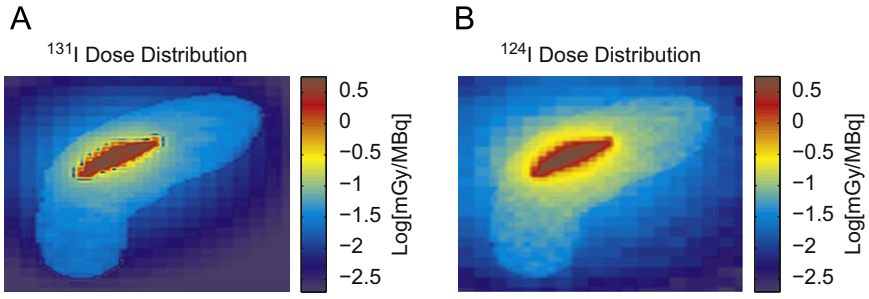

Fig. 4. The figures illustrate the voxel dose distributions of ^{124}I and ^{131}I and within axial slices of the liver and tumor. Notice how much higher the tumor dose is in comparison to the normal liver. When considering (A) and (B), both ^{124}I and ^{131}I contribute dose to the neighboring organs but ^{124}I contributes significantly more. This is a very important point when comparing the three dimensional dosimetry of the two radionuclides.

Table 2
The average BED of ^{124}I and ^{131}I in the liver and tumor in units of $(mGy/MBq)_{inj}$ of NM404.

$(mGy/MBq)_{inj}$ NM404	Liver	Tumor	Tumor/liver ratio
^{124}I	0.031	1.2	39
^{131}I	0.022	1.5	68

Table 3
The top section shows BED dose from 370 MBq of ^{124}I. The bottom section shows BED from ^{131}I therapy.

	$(mGy/MBq)_{inj}$ NM404	Dose (mGy)
^{124}I-NM404 imaging		
Liver (1/3)	0.025	9.3
Tumor (3/3)	0.420	156
^{131}I-NM404 therapy		
Liver (1/3)	0.017	$BED_{5/5}$ 1/3=6200
Tumor (3/3)	0.230	8400

The dose at 1/3 volume was used for the liver while the dose at 3/3 volume was used for the tumor (Fig. 3).

Fig. 3 provides the information needed for the treatment planning step. As indicated in Table 3, the volumes of interest were 33% and 100% for the liver and tumor, respectively.

To avoid liver toxicity of $BED_{5/5}$ 1/3 of 62 Gy, the maximum permissible injected ^{131}I was 3.65×10^5 MBq. From (8), this results in a tumor BED of 84 Gy which is tumorcidal.

$$Tumor\ \ dose_{BED} = A_{\max} \cdot Tumor\left[\frac{\text{mGy}}{\text{MBq}_{^{131}I}}\right] \tag{8}$$

4. Discussion

A very important assumption when doing patient specific dosimetry for treatment planning is that the distribution of the radiotherapy nuclide is synonymous to that of the PET isotope. When this is assumed, it is possible to compute three dimensional voxel based dosimetry for radiation treatment planning of systemically administered radiopharmaceuticals based on *a priori* imaging data. It is apparent from Table 2 that ^{124}I has a comparable tumor dose to that of ^{131}I which demonstrates that during treatment planning it is useful to include the absorbed dose due to diagnostic imaging. Fig. 3 shows that ^{124}I delivers a more uniform tumor dose but achieves less maximum doses compared to ^{131}I. This is due to the fact that ^{124}I emits positrons which have a comparable absorbed dose to beta rays from ^{131}I. Despite this, the tumor-to-liver ratio is considerably less compared to ^{131}I because ^{124}I distributes more of its energy at further distances compared to ^{131}I (Furhang et al., 1996). This causes ^{131}I to be more protective of the liver than ^{124}I and is thus a better therapeutic agent (Fig. 3). Overall, the use of ^{124}I for imaging and ^{131}I for radiotherapy was reiterated.

When comparing absorbed dose to BED, it is interesting to note that the lower dose-rate of radionuclide therapy acts to spare the liver. According to Emami, the $TD_{5/5}$ of 1/3 liver is 50 Gy for external beam therapy. In this study of ^{131}I therapy, the $BED_{5/5}$ of 1/3 liver was raised to 62 Gy. This increase in allowable liver dose indirectly increased the BED for the tumor as well from 68 to 84 Gy, absorbed dose and BED, respectively. In addition, when considering BED instead of absorbed dose, the tumor:liver ratio (Table 2) increased from 65 to 68, respectively.

When comparing the liver and tumor doses, it needs to be emphasized that the tumor's pharmacokinetics were simulated to be exactly the same as the liver's pharmacokinetics which ultimately lead to an incorrect assumption about effective tumor clearance (λ_{eff}). Thus, when considering an injected amount of activity, 1 MBq in this case, it was possible to calculate dose using the given MCNPX set-up. The accumulated activity within the liver is different from that of the tumor due to the fact that the tumor started with 15% of the injected activity while the liver had 6.5%. Physiologically, each has different biological clearance constants (λ_{bio}) which would contribute to even greater differences in accumulated activities. Because the pharmacokinetics of the tumor and liver possess different clearance constants, it is necessary to have a source definition in MCNPX that not only varied with location and energy, but also time. Regardless of this limitation, the methodology that the authors established could be applied to future studies of different tumor types and locations for treatment planning purposes.

The greatest uncertainty associated with this study is found in the PET imaging. One downfall was that the patient was only injected with 1.5 mCi of ^{124}I. To put this into perspective, a patient undergoing a ^{18}F-FDG scan usually is injected with approximately 10 mCi to ensure diagnostic quality. Furthermore, ^{18}F emits almost four times more positrons than ^{124}I which further emphasizes the lack of detectable radioactive decays that were present in our study. Because PET follows Poisson statistics, the signal-to-noise ratio follows $N/\sqrt{N}$ (where N=counts) which means that less than adequate counts introduces noise to the image which increases its uncertainty. A study by Jentzen et al. (2008) showed that even when corrections are applied to ^{124}I images, there is a $\pm$10% inaccuracy. They suggest performing a recovery correction of the data when using ^{124}I for estimating ^{131}I dosimetry of which was not performed in our study.

The uncertainty in the Monte Carlo process is minimized by simulating a high number of particles as to reduce the variance within each voxel. Another possibility is increasing the voxel size but that diminishes the dose resolution. The conversion of the

PET/CT data into the Monte Carlo environment via SCMS does not introduce any foreseeable uncertainty. However, we did not benchmark our methodology by comparing our results to reference dose distributions.

5. Conclusions

Using SCMS to convert PET/CT data into the MCNPX environment allowed for a precise voxel based dosimetry of a tumor within the liver. Though the application was limited to only two physiological structures, the methodology demonstrates the ability of using Monte Carlo simulation aided by PET/CT data to do patient specific dosimetry for treatment planning of radioiodinated pharmaceuticals. With the improvement in computer processing speed, Monte Carlo is becoming a mainstay in nuclear medicine and should be explored for use in other biomedical applications. In this particular application, we showed that ^{124}I delivers comparable tumor dose to ^{131}I but has the propensity of distributing its dose to neighboring organs. Because ^{131}I is more normal tissue sparing, it has a higher therapeutic index which makes it a better therapeutic agent.

Disclosure

Jamey Weichert is a cofounder of Cellectar, Inc. which holds the licensing rights to NM404.

References

Bai, C., Kinahan, P.E., Brasse, D., Comtat, C., Townsend, D.W., Meltzer, C.C., Villemagne, V., Charron, M., Defrise, M., 2003. An analytic study of the effects of attenuation on tumor detection in whole-body PET oncology imaging. Journal of Nuclear Medicine 44, 1855–1861.

Barone, R., Borson-Chazot, F., Valkema, R., Walrand, S., Chauvin, F., Gogou, L., Kvols, L.K., Krenning, E.P., Jamar, F., Pauwels, S., 2005. Patient-specific dosimetry in predicting renal toxicity with (90)Y-DOTATOC: relevance of kidney volume and dose rate in finding a dose-effect relationship. Journal of Nuclear Medicine 46 (Suppl. 1), 99S–106S.

Bodey, R.K., Evans, P.M., Flux, G.D., 2004. Application of the linear-quadratic model to combined modality radiotherapy. International Journal of Radiation Oncology, Biology, Physics 59, 228–241.

Brans, B., Bodei, L., Giammarile, F., Linden, O., Luster, M., Oyen, W.J., Tennvall, J., 2007. Clinical radionuclide therapy dosimetry: the quest for the Holy Gray. European Journal of Nuclear Medicine and Molecular Imaging 34, 772–786.

Breitz, H., Wendt, R., Stabin, M., Bouchet, L., Wessels, B., 2003. Dosimetry of high dose skeletal targeted radiotherapy (STR) with 166Ho-DOTMP. Cancer Biotherapy & Radiopharmaceuticals 18, 225–230.

Brenner, D.J., Hlatky, L.R., Hahnfeldt, P.J., Huang, Y., Sachs, R.K., 1998. The linear-quadratic model and most other common radiobiological models result in similar predictions of time–dose relationships. Radiation Research 150, 83–91.

Brown, S., Bailey, D.L., Willowson, K., Baldock, C., 2008. Investigation of the relationship between linear attenuation coefficients and CT Hounsfield units using radionuclides for SPECT. Applied Radiation and Isotopes 66, 1206–1212.

Dale, R., Carabe-Fernandez, A., 2005. The radiobiology of conventional radiotherapy and its application to radionuclide therapy. Cancer Biotherapy & Radiopharmaceuticals 20, 47–51.

Dale, R.G., 1985. The application of the linear-quadratic dose-effect equation to fractionated and protracted radiotherapy. British Journal of Radiology 58, 515–528.

Dale, R.G., 1989. Radiobiological assessment of permanent implants using tumour repopulation factors in the linear-quadratic model. British Journal of Radiology 62, 241–244.

Dale, R.G., 1996. Dose-rate effects in targeted radiotherapy. Physics in Medicine and Biology 41, 1871–1884.

Delbeke, D., Schoder, H., Martin, W.H., Wahl, R.L., 2009. Hybrid imaging (SPECT/CT and PET/CT): improving therapeutic decisions. Seminars in Nuclear Medicine 39, 308–340.

Dewaraja, Y.K., Wilderman, S.J., Koral, K.F., Kaminski, M.S., Avram, A.M., 2009. Use of integrated SPECT/CT imaging for tumor dosimetry in I-131 radioimmunotherapy: a pilot patient study. Cancer Biotherapy & Radiopharmaceuticals 24, 417–426.

Dingli, D., Kemp, B.J., O'Connor, M.K., Morris, JC., Russell, S.J., Lowe, V.J., 2006. Combined I-124 positron emission tomography/computed tomography imaging of NIS gene expression in animal models of stably transfected and intravenously transfected tumor. Molecular Imaging and Biology 8, 16–23.

Doll, J., Henze, M., Bublitz, O., Werling, A., Adam, L.E., Haberkorn, U., Semmler, W., Brix, G., 2004. High resolution reconstruction of PET images using the iterative OSEM algorithm. Nuklearmedizin 43, 72–78.

Emami, B., Lyman, J., Brown, A., Coia, L., Goitein, M., Munzenrider, J.E., Shank, B., Solin, L.J., Wesson, M., 1991. Tolerance of normal tissue to therapeutic irradiation. International Journal of Radiation Oncology, Biology, Physics 21, 109–122.

Eschmann, S.M., Reischl, G., Bilger, K., Kupferschlager, J., Thelen, M.H., Dohmen, B.M., Besenfelder, H., Bares, R., 2002. Evaluation of dosimetry of radioiodine therapy in benign and malignant thyroid disorders by means of iodine-124 and PET. European Journal of Nuclear Medicine and Molecular Imaging 29, 760–767.

Ferrari, P., Gualdrini, G., 2007. Mcnpx internal dosimetry studies based on the norman-05 Voxel model. Radiation Protection Dosimetry 127(1–4), 209–213.

Flux, G., Bardies, M., Monsieurs, M., Savolainen, S., Strands, S.E., Lassmann, M., 2006. The impact of PET and SPECT on dosimetry for targeted radionuclide therapy. Zeitschrift fur medizinische Physik 16, 47–59.

Furhang, E.E., Sgouros, G., Chui, C.S., 1996. Radionuclide photon dose kernels for internal emitter dosimetry. Medical Physics 23, 759–764.

Gear, J.I., Charles-Edwards, E., Partridge, M., Flux, G.D., 2007. A quality-control method for SPECT-based dosimetry in targeted radionuclide therapy. Cancer Biotherapy & Radiopharmaceuticals 22, 166–174.

Hobbs, R.F., Sgouros, G., 2009. Calculation of the biological effective dose for piecewise defined dose-rate fits. Medical Physics 36, 904–907.

Jentzen, W., Weise, R., Kupferschlager, J., Freudenberg, L., Brandau, W., Bares, R., Burchert, W., Bockisch, A., 2008. Iodine-124 PET dosimetry in differentiated thyroid cancer: recovery coefficient in 2D and 3D modes for PET(/CT) systems. European Journal of Nuclear Medicine and Molecular Imaging 35, 611–623.

Kinahan, P.E., Townsend, D.W., Beyer, T., Sashin, D., 1998. Attenuation correction for a combined 3D PET/CT scanner. Medical Physics 25, 2046–2053.

Lazarescu, G.R., Battista, J.J., 1997. Analysis of the radiobiology of ytterbium-169 and iodine-125 permanent brachytherapy implants. Physics in Medicine and Biology 42, 1727–1736.

MATLAB, 2006. The MathWorks, Natick, MA.

Millar, W.T., 1991. Application of the linear-quadratic model with incomplete repair to radionuclide directed therapy. British Journal of Radiology 64, 242–251.

O'Donoghue, J.A., Baidoo, N., Deland, D., Welt, S., Divgi, C.R., Sgouros, G., 2002. Hematologic toxicity in radioimmunotherapy: dose-response relationships for I-131 labeled antibody therapy. Cancer Biotherapy & Radiopharmaceuticals 17, 435–443.

O'Donoghue, J.A., Wheldon, T.E., 1996. Targeted radiotherapy using Auger electron emitters. Physics in Medicine and Biology 41, 1973–1992.

Ott, R.J., 1996. Imaging technologies for radionuclide dosimetry. Physics in Medicine and Biology 41, 1885–1894.

Pauwels, S., Barone, R., Walrand, S., Borson-Chazot, F., Valkema, R., Kvols, L.K., Krenning, E.P., Jamar, F., 2005. Practical dosimetry of peptide receptor radionuclide therapy with (90)Y-labeled somatostatin analogs. Journal of Nuclear Medicine 46 (Suppl. 1), 92S–98S.

Pentlow, K.S., Graham, M.C., Lambrecht, R.M., Cheung, N.K., Larson, S.M., 1991. Quantitative imaging of I-124 using positron emission tomography with applications to radioimmunodiagnosis and radioimmunotherapy. Medical Physics 18, 357–366.

Pinchuk, A.N., Rampy, M.A., Longino, M.A., Skinner, R.W., Gross, M.D., Weichert, J.P., Counsell, R.E., 2006. Synthesis and structure–activity relationship effects on the tumor avidity of radioiodinated phospholipid ether analogues. Journal of Medicinal Chemistry 49, 2155–2165.

Rahmim, A., Zaidi, H., 2008. PET versus SPECT: strengths, limitations and challenges. Nuclear Medicine Communications 29, 193–207.

Rault, E., Vandenberghe, S., Van Holen, R., De Beenhouwer, J., Staelens, S., Lemahieu, I., 2007. Comparison of image quality of different iodine isotopes (I-123, I-124, and I-131). Cancer Biotherapy & Radiopharmaceuticals 22, 423–430.

Ravinder, K.G., Mark, L., Keith, S.P., Steven, M.L., 2007. The role of iodine-124-positron emission tomography imaging in the management of patients with thyroid cancer. PET Clinics 2, 313–320.

Roberson, P.L., Buchsbaum, D.J., 1995. Reconciliation of tumor dose response to external beam radiotherapy versus radioimmunotherapy with 131iodine-labeled antibody for a colon cancer model. Cancer Research 55, 5811s–5816s.

Sachs, R.K., Hahnfeld, P., Brenner, D.J., 1997. The link between low-LET dose-response relations and the underlying kinetics of damage production/repair/misrepair. International Journal of Radiation Biology 72, 351–374.

Sgouros, G., Kolbert, K.S., Sheikh, A., Pentlow, K.S., Mun, E.F., Barth, A., Robbins, R.J., Larson, S.M., 2004. Patient-specific dosimetry for 131I thyroid cancer therapy using 124I PET and 3-dimensional-internal dosimetry (3D-ID) software. Journal of Nuclear Medicine 45, 1366–1372.

Stabin, M.G., da Luz, L.C., 2002. Decay data for internal and external dose assessment. Health Physics 83, 471–475.

Stabin, M.G., Sparks, R.B., Crowe, E., 2005. OLINDA/EXM: the second-generation personal computer software for internal dose assessment in nuclear medicine. Journal of Nuclear Medicine 46, 1023–1027.

Strand, S.E., Zanzonico, P., Johnson, T.K., 1993. Pharmacokinetic modeling. Medical Physics 20, 515–527.

Thomas, S.R., 2002. Options for radionuclide therapy: from fixed activity to patient-specific treatment planning. Cancer Biotherapy & Radiopharmaceuticals 17, 71–82.

Weichert, J.P., Moser, A.R., Weber, S.M., Qi, C., Longino, M.A., 2005. Radioiodinated NM404—a universal tumor imaging agent. Academic Radiology 12, S58–S59.

Williams, L.E., DeNardo, G.L., Meredith, R.F., 2008. Targeted radionuclide therapy. Medical Physics 35, 3062–3068.

Yang, Y., Xing, L., 2005. Optimization of radiotherapy dose-time fractionation with consideration of tumor specific biology. Medical Physics 32, 3666–3677.

Yoriyaz, H., Stabin, M.G., dos Santos, A., 2001. Monte Carlo MCNP-4B-based absorbed dose distribution estimates for patient-specific dosimetry. Journal of Nuclear Medicine 42, 662–669.